




Tunable Aharonov-Bohm cages through anti- \mathcal{PT} -symmetric imaginary couplingsS. M. Zhang ^{*}, H. S. Xu ^{*}, and L. Jin [†]*School of Physics, Nankai University, Tianjin 300071, China*

(Received 27 April 2023; revised 28 July 2023; accepted 3 August 2023; published 21 August 2023)

The Aharonov-Bohm (AB) cage enables localized confinement with nondiffractive propagation for arbitrary excitation. In this study, we introduce an anti-parity-time (anti- \mathcal{PT}) symmetric imaginary coupling in a generalized Creutz ladder to construct a non-Hermitian AB cage with tunable flat-band energy. We investigate compact localized states and complete localization dynamics, and show that non-Hermiticity affects the localization probability distributions and increases the oscillation period of the AB cage dynamics. Non-Hermitian engineering of the decoupled core of the AB cage is the essential point in our proposal. Our approach is widely applicable to a more general situation and can facilitate the manipulation of localization in physics.

DOI: [10.1103/PhysRevA.108.023518](https://doi.org/10.1103/PhysRevA.108.023518)**I. INTRODUCTION**

Flat bands are a peculiar category of band structure that have fixed energies independent of the crystal momentum [1,2]. They arise from destructive interference in many physical systems [3–7], and possess the unique property that the electron group velocity is exactly zero. This property gives rise to various exotic phenomena in many-body physics [8–10]. In addition, the eigenstates of the flat bands, known as compact localized states (CLSs), are completely localized in one or more finite unit cells [11–13]. This prevents the wave transport and makes it possible to trap and steer the propagation of light on a given region [14,15]. However, the perfectly localized modes will be destroyed after the introduction of nonlinearity [15]. In addition, some of flat-band systems can exhibit interesting transport [16,17]; in particular, the direction of transport can be well controlled according to the excitation site or input phase in a rhombic lattice [18]. In addition, the dispersionless nature of the flat-band systems make them guarantee a greatly enhanced density of states, which amplifies the effects of interactions. As a result, minimal repulsive on-site interactions can lead to superconductivity [19–21]. Moreover, extensive theoretical works have demonstrated the topological properties of nearly flat-band systems supporting unusual fractional topological phases [22–25]. The intriguing physics associated with flat bands has motivated their experimental realization in various one-dimensional and two-dimensional settings, including optical waveguides [26–29], cold atomic gases in optical lattices [30–32], and metamaterials [33–37]. Recently, research

interest in flat bands continuously increased in optics [38], condensed matters, and material science. In particular, the flat-band localization in the Creutz ladder can be finely controlled in the superradiance lattices [39].

Stemming from the competition between geometry and magnetic fields, the Aharonov-Bohm (AB) cage is a special flat-band system with its energy bands fully flat. Any excitation in the system is completely confined to a certain region. In the presence of a magnetic π flux (i.e., half a flux quantum) per plaquette, the quasi-one-dimensional (quasi-1D) rhombic lattice [40,41] and the two-dimensional dice lattice [42–46] are celebrated models that support the AB cages and have drawn much attention. Advanced fabrication techniques allow these models to be realized in the laboratory. A total flux of π within each plaquette of the rhombic waveguide lattice was obtained by introducing the effective coupling between different orbital modes [18], inserting an auxiliary waveguide in each plaquette [47], or injecting the light beam with an orbital angular momentum [48]. The importance of the AB cage is reflected in many aspects [49–51], ranging from topological edge states [52] to flat-band lasers [53]. The presence of nonlinearity or interactions in the Creutz ladder has attracted much attention [54–56]. Disorder on the Creutz ladder with interparticle interactions induces exotic many-body localization dynamics [57], while the repulsive Hubbard interaction causes repulsively bound pairs in the photonic Creutz-Hubbard ladder [58].

In recent decades, the non-Hermitian systems have been widely investigated both theoretically and experimentally due to their intriguing properties [59–62], including exceptional points (EPs) [63,64], unique light transport and wave propagation [65–67], and exotic topology [68–71]. As interest in non-Hermitian systems continues to grow, proposals for flat bands have emerged in a large number of non-Hermitian systems [72–85]. Non-Hermitian flat bands can exhibit polynomial power increase of flat-band eigenstates [72,76], which have no counterpart in Hermitian cases. However, most of these studies focused on the flat bands created at the EPs [83–85].

^{*}These authors contributed equally to this work.

[†]jinliang@nankai.edu.cn

Published by the American Physical Society under the terms of the Creative Commons Attribution 4.0 International license. Further distribution of this work must maintain attribution to the author(s) and the published article's title, journal citation, and DOI.

In this study, we propose a mechanism for fabricating a non-Hermitian AB cage that is not necessarily at the EP of the non-Hermitian lattice. This is distinct from previous non-Hermitian AB cages that are formed exactly at the EP of the non-Hermitian lattice. We introduce an approach to properly incorporate non-Hermiticity into the Hermitian AB cage to keep all the bands flat, thus creating the non-Hermitian AB cage. We demonstrate our proposal using a generalized cross-stitch lattice. The anti-parity-time (anti- \mathcal{PT}) symmetric imaginary coupling between two sublattices of the generalized cross-stitch lattice forms a non-Hermitian Creutz ladder with a fully flat spectrum. In the time-evolution dynamics, the excitation is fully confined inside the nearest-neighbor unit cells, and the intensity of confinement can exhibit constant, oscillating, and exponential growth at different degrees of non-Hermiticity. At weak imaginary coupling strength, the flat-band spectrum is entirely real; at strong imaginary coupling strength, the flat-band spectrum is entirely imaginary. The non-Hermiticity extends the period of oscillation when the spectrum is real, and causes the probability distribution of the confined excitation to pile up when the spectrum is imaginary.

The remainder of the paper is organized as follows. In Sec. II, we introduce the generalized cross-stitch lattice, present the flat bands, and demonstrate the confinement mechanism. In Sec. III, we propose the non-Hermitian Creutz ladder by introducing dissipation-induced imaginary couplings, and demonstrate the CLSs of the non-Hermitian AB cage not at the EP. In Sec. IV, we analyze the typical localization dynamics in the non-Hermitian cage. In Sec. V, we discuss the experimental implementation of the proposed non-Hermitian AB cage in the coupled resonator optical waveguides. Our conclusions and discussions are summarized in Sec. VI.

II. CROSS-STITCH LATTICE

Figure 1(a) schematically illustrates a generalization of the conventional cross-stitch lattice [86]. Each coupling $\pm iJ/2$ has a nonreciprocal Peierls phase factor $e^{\pm i\pi/2}$. The sign \pm of the nonreciprocal coupling $\pm iJ/2$ depends on the tunneling direction of the particles. The particles tunneling along the black arrow acquire a Peierls phase factor $e^{i\pi/2}$ while the particles tunneling against the black arrow acquire a Peierls phase factor $e^{-i\pi/2}$. The cross-stitch lattice can be viewed as sharing the same geometry as two rhombic chains [58], or alternatively, as the Creutz ladder without rungs.

In spatial space, the Hamiltonian of the generalized cross-stitch lattice is written in the form of

$$H = \sum_n [(iJ/2)b_n^\dagger(a_{n+1} + b_{n+1}) - (iJ/2)a_n^\dagger(a_{n+1} + b_{n+1})] + \text{H.c.}, \quad (1)$$

where a_n^\dagger (a_n) and b_n^\dagger (b_n) represent the creation (annihilation) operators of the sublattices A and B , respectively. The lattice is translationally invariant in the horizontal direction. The j th unit cell of the generalized cross-stitch lattice includes two sites A_j and B_j . Notably, the generalized cross-stitch lattice is Hermitian and does not include any intracell coupling.

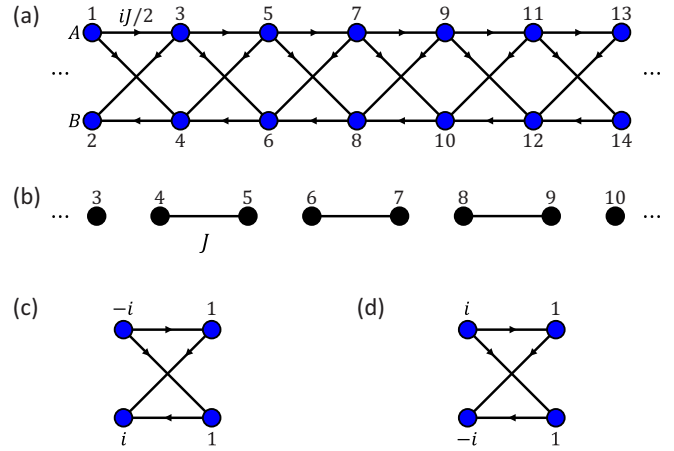


FIG. 1. (a) Schematic of the Hermitian cross-stitch lattice. (b) Equivalent lattice of decoupled dimers obtained by applying a similar transformation to (a). The reciprocal coupling strength is J . (c) Compact localized eigenstate with the positive flat-band energy J . (d) Compact localized eigenstate with the negative flat-band energy $-J$. The site numbers in (a) correspond to those in (b) under a similar transformation.

In momentum space, the Bloch Hamiltonian under Fourier transformation is written in the form of

$$H_k = (J \cos k)\sigma_y + (J \sin k)\sigma_z, \quad (2)$$

where $\sigma_{x,y,z}$ is the Pauli matrix for the spin-1/2. The energy bands $E_k = \pm J$ of H_k are dispersionless and independent of the momentum k . Therefore, the generalized cross-stitch lattice possesses an entirely flat spectrum and supports an AB cage.

Now, we introduce an equivalent lattice as shown in Fig. 1(b) to illustrate the kernel of the AB cage in the generalized cross-stitch lattice. The schematic provides a concise and clear physical picture to depict the essential feature of the generalized cross-stitch lattice. The Hamiltonian H' of the equivalent lattice is connected to the Hamiltonian H of the generalized cross-stitch lattice under a similar transformation $H' = UH U^{-1}$. The most intriguing fact about the equivalent lattice is the decoupled dimerization. This generally originates from the distractive interference between the hoppings. Figure 1(b) illustrates the equivalent lattice H' of the generalized cross-stitch lattice, which is fully constituted by the decoupled dimers. Each dimer including a reciprocal coupling J and all the dimers are identical. Thus, the spectrum of the proposed AB cage is composed of two flat bands $\pm J$ and the eigenstates are definitely localized in each isolated dimer of the equivalent lattice. Notably, the equivalence to a lattice of decoupled polymers is a feature for any AB cage from the fact that all the bands are flat. From the equivalent lattice, we easily obtain the confinement of the original AB cage. This also helps to further engineering the AB cage and the confinement.

As a result, the corresponding eigenstates of the generalized cross-stitch lattice are also compactly localized. Both CLSs of the generalized cross-stitch lattice in Fig. 1(a) are distributed and confined in a four-site plaquette configuration. These CLSs are obtained from the steady-state Schrödinger equations. The CLS is $[-i, i, 1, 1]^T/2$ for the flat-band energy

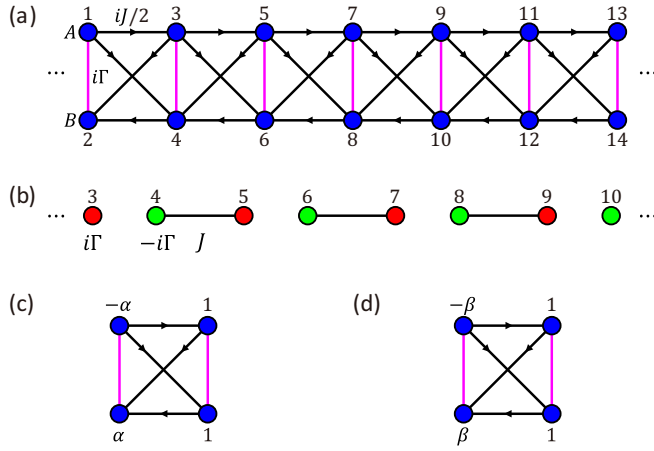


FIG. 2. (a) Schematic of the non-Hermitian Creutz ladder to construct the AB cage not at the EP. Reciprocal non-Hermitian couplings $i\Gamma$ present in the vertical direction. (b) Schematic of the equivalent chain. The non-Hermitian dimers are obtained by adding gain $+i\Gamma$ (red) and loss $-i\Gamma$ (green) to Fig. 1(b). (c) Compact localized eigenstate with the flat-band energy $\sqrt{J^2 - \Gamma^2}$. (d) Compact localized eigenstate with the flat-band energy $-\sqrt{J^2 - \Gamma^2}$. The signs in (c) and (d) are $\alpha = (\Gamma - \sqrt{\Gamma^2 - J^2})/J$, $\beta = (\Gamma + \sqrt{\Gamma^2 - J^2})/J$.

J [Fig. 1(c)] and the CLS is $[i, -i, 1, 1]^T$ for the flat-band energy $-J$ [Fig. 1(d)]. The localization of the CLSs is attributed to destructive interference.

The conventional cross-stitch lattice is similar to the generalized configuration in Fig. 1(a), except that the phase factor $e^{\pm i\pi/2}$ only sticks to the upper and lower chains. The cross couplings $J/2$ between sublattices A and B maintain the two flat energy bands $\pm J$ [87], with both interchain and intrachain hopping amplitudes set to $J/2$. The absence or presence of the phase factor $e^{\pm i\pi/2}$ in the cross couplings is the only difference between the conventional and generalized cross-stitch lattices. Both types of cross-stitch lattices originate from the same equivalent lattice as shown in Fig. 1(b). However, additional intracell couplings $\sum_n (e^{i\pi/2} \Omega a_n^\dagger b_n + e^{-i\pi/2} \Omega b_n^\dagger a_n)$ between sublattices in the vertical direction significantly alter the flat bands. Adding intracell couplings to the conventional cross-stitch lattice extends it into a four-flat-band Creutz ladder, with the four flat-band energies being $\pm J \pm \Omega$ [88]. By contrast, adding the vertical coupling Ω between sublattices to the generalized cross-stitch lattice results in a two-band Creutz ladder, with the two flat-band energies being $\pm\sqrt{J^2 + \Omega^2}$. The subtly designed phase factor in the cross couplings $\pm iJ/2$ of the generalized configuration in Fig. 1(a) plays a critical role in maintaining the two-band structure. Imaginary (real) vertical couplings decrease (increase) the band gap of the non-Hermitian (Hermitian) Creutz ladder. In an interacting system, large repulsive interactions in the Creutz ladder generate oscillating behavior in the local integrals of motion [57].

III. NON-HERMITIAN CREUTZ LADDER

Figure 2(a) shows the non-Hermitian Creutz ladder with imaginary couplings introduced between two ladder legs [89]. The intracell couplings $i\Gamma$ are reciprocal, while the intercell couplings $\pm iJ/2$ are nonreciprocal. The real-space

Hamiltonian of the non-Hermitian Creutz ladder reads

$$\begin{aligned} \mathcal{H} = & \sum_n -\frac{iJ}{2} a_n^\dagger (a_{n+1} + b_{n+1}) + \text{H.c.} \\ & + \sum_n \frac{iJ}{2} b_n^\dagger (a_{n+1} + b_{n+1}) + \text{H.c.} \\ & + \sum_n i\Gamma a_n^\dagger b_n + i\Gamma b_n^\dagger a_n. \end{aligned} \quad (3)$$

The imaginary coupling, satisfying the anti- \mathcal{PT} symmetry [70,90,91], has been experimentally realized in various systems such as the optical microcavity [92], coupled waveguides [93], optical fibers [94], heat diffusion systems [95], cavity magnonics [96,97], cold atoms [98,99], electrical circuit resonators [100–102], and quantum systems [103]. The flying atoms with ground-state coherence indirectly account for the imaginary couplings through coherently mixed spin waves [104]. Two setups, one consisting of a spinning resonator driven by a pair of lasers propagating in opposite directions [105] and the other comprising a series of parallel cascaded resonators [106], have already induced the imaginary coupling. The auxiliary waveguides can be adiabatically eliminated to realize the effective imaginary coupling in a coupled waveguide array with alternately arranged auxiliary and primary waveguides [107–109]. Additionally, a photonic system consisting of two microresonators connected with two common waveguides is accessible to obtain the dissipative coupling. The effective Hamiltonian of this setup, expressed as a 2×2 matrix, is reduced from the Heisenberg-Langevin equations of microresonator modes. The indirect coupling between microresonators indicated by nondiagonal terms of the effective Hamiltonian is $-ie^{i\delta}\Gamma$, with the microresonator-waveguide coupling Γ and propagation phase factor of the probe light $e^{i\delta}$. When considering $\delta = \pm\pi$, the reciprocal indirect coupling $-ie^{\pm i\pi}\Gamma$ is anti- \mathcal{PT} symmetric and is free of the gain-loss match in \mathcal{PT} symmetry. Here, we concentrate on the imaginary coupling $i\Gamma$.

Figure 2(b) shows an equivalent non-Hermitian dimerized chain. Additional imaginary couplings $i\Gamma$ in Fig. 2(a) yield additional gain and loss $\pm i\Gamma$ in each isolated dimer of Fig. 2(b). The non-Hermitian generalization maintains the AB cage, but affects the flat-band energy and localization dynamics. We further elaborate on the non-Hermitian isolation to proceed with our discussion. The gain and loss $i\Gamma\sigma_z$ relate to the imaginary coupling $i\Gamma\sigma_x$ through a similar transformation

$$\begin{pmatrix} i & i \\ -1 & 1 \end{pmatrix}^{-1} \begin{pmatrix} i\Gamma & 0 \\ 0 & -i\Gamma \end{pmatrix} \begin{pmatrix} i & i \\ -1 & 1 \end{pmatrix} = \begin{pmatrix} 0 & i\Gamma \\ i\Gamma & 0 \end{pmatrix}. \quad (4)$$

The non-Hermitian Creutz ladder in Fig. 2(a) is obtained by applying the inverse similar transformation to the non-Hermitian dimerized lattice in Fig. 2(b). In this situation, the Bloch Hamiltonian of the non-Hermitian Creutz ladder in momentum space reads

$$\mathcal{H}_k = \begin{pmatrix} J \sin k & i\Gamma - iJ \cos k \\ i\Gamma + iJ \cos k & -J \sin k \end{pmatrix}. \quad (5)$$

The band energies $E_k = \pm\sqrt{J^2 - \Gamma^2}$ of \mathcal{H}_k are independent of the momentum k , and the imaginary coupling Γ narrows

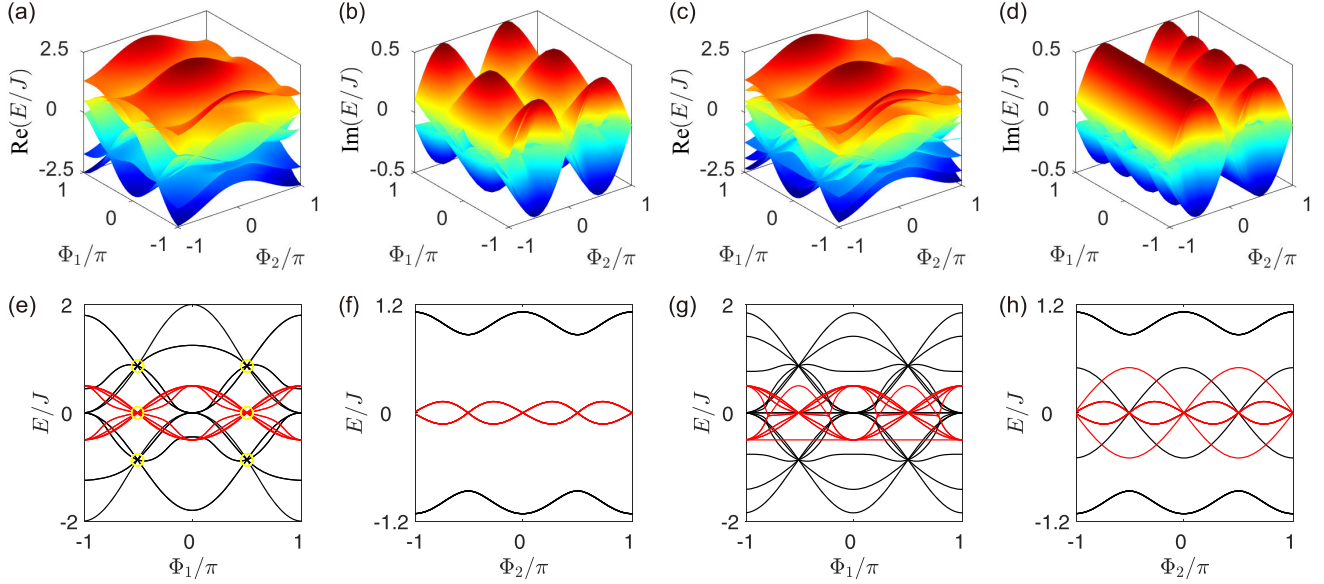


FIG. 3. Spectra of the real-space non-Hermitian Creutz ladder under periodic boundary condition [(a), (b), (e), (f)] and open boundary condition [(c), (d), (g), (h)]. The phase $\Phi_2 = \pi/2$ is set in (e) and (g), causing a large number of energy levels coalesce to two real energies indicated by yellow circles, where the AB cage forms. In (f), $\Phi_1 = \pi/2$, both bands are flat as Φ_2 changes. The real (imaginary) part in the four lower panels is depicted in black (red). The Creutz ladder has $N = 7$ unit cells, with $J = 1$ and $\Gamma = 1/2$.

the band gap. We notice that the non-Hermitian AB cage is not at the EP except for $J = \Gamma$. This is a prominent difference from the non-Hermitian AB cages proposed exactly at the EP, where the isolated dimers are unidirectionally coupled [73,79,85]. However, all the energy levels of the non-Hermitian Creutz ladder are two-state coalesced at $J = \Gamma$.

Next, we discuss the eigenenergies and eigenstates of the non-Hermitian Creutz ladder. We plot the eigenenergies of a 14-site Creutz ladder in Fig. 3, where the nonreciprocal couplings $\pm iJ/2$ are substituted by $e^{\pm i\Phi_1}J/2$ and the reciprocal couplings $i\Gamma$ are substituted by $e^{i\Phi_2}\Gamma$. The AB cage forms at $\Phi_1 = \pi/2$ and is clearly exhibited in Fig. 3(e). We also show the wave-function amplitudes of CLSs in Figs. 2(c) and 2(d). The discrete Schrödinger equations for the non-Hermitian Creutz ladder are

$$i\dot{\psi}_{A_j} = i\Gamma\psi_{B_j} - iJ/2\psi_{A_{j+1}} - iJ/2\psi_{B_{j+1}} + iJ/2\psi_{A_{j-1}} - iJ/2\psi_{B_{j-1}}, \quad (6)$$

$$i\dot{\psi}_{B_j} = i\Gamma\psi_{A_j} + iJ/2\psi_{A_{j+1}} + iJ/2\psi_{B_{j+1}} + iJ/2\psi_{A_{j-1}} - iJ/2\psi_{B_{j-1}}, \quad (7)$$

where ψ_{A_j} and ψ_{B_j} are the wave functions at the j th unit cell of the Creutz ladder. It is straightforward to verify that the two CLSs shown in Figs. 2(c) and 2(d) are the steady-state solutions, and the wave functions outside the square plaquettes are zero.

IV. NON-HERMITIAN LOCALIZATION DYNAMICS

The most significant and intriguing property of the non-Hermitian Creutz ladder is the excitation confinement. The non-Hermitian localization dynamics is solely induced by the intracell imaginary coupling, including constant, oscillating, and increasing excitation intensities. Both bounded and unbounded excitation intensities are compactly localized in finite

sites as a consequence of the localization of the CLSs. In this section, we concentrate on the localization dynamics of the non-Hermitian Creutz ladder for different excitations under open boundary condition.

We analyze the localization dynamics of a single-site excitation from an analytical perspective. The excitation at sublattice A and the excitation at sublattice B are two types of single-site excitations in the non-Hermitian Creutz ladder. The localization dynamics is inevitable for any excitation due to the fully flat spectrum. Any single-site excitation is completely confined within six sites, as the initial state labeled $\psi_1(0) = [0, 0, 1, 0, 0, 0]^T$ can be expressed as a superposition of four CLSs

$$\begin{aligned} \psi_1(0) = & -\frac{\beta}{2\alpha - 2\beta}[-\alpha, \alpha, 1, 1, 0, 0]^T \\ & + \frac{\alpha}{2\alpha - 2\beta}[-\beta, \beta, 1, 1, 0, 0]^T \\ & - \frac{1}{2\alpha - 2\beta}[0, 0, -\alpha, \alpha, 1, 1]^T \\ & + \frac{1}{2\alpha - 2\beta}[0, 0, -\beta, \beta, 1, 1]^T. \end{aligned} \quad (8)$$

Similarly, the superposition coefficients of the initial state $\psi_2(0) = [0, 0, 0, 1, 0, 0]^T$ are given in the form of

$$\begin{aligned} \psi_2(0) = & -\frac{\beta}{2\alpha - 2\beta}[-\alpha, \alpha, 1, 1, 0, 0]^T \\ & + \frac{\alpha}{2\alpha - 2\beta}[-\beta, \beta, 1, 1, 0, 0]^T \\ & + \frac{1}{2\alpha - 2\beta}[0, 0, -\alpha, \alpha, 1, 1]^T \\ & - \frac{1}{2\alpha - 2\beta}[0, 0, -\beta, \beta, 1, 1]^T. \end{aligned} \quad (9)$$

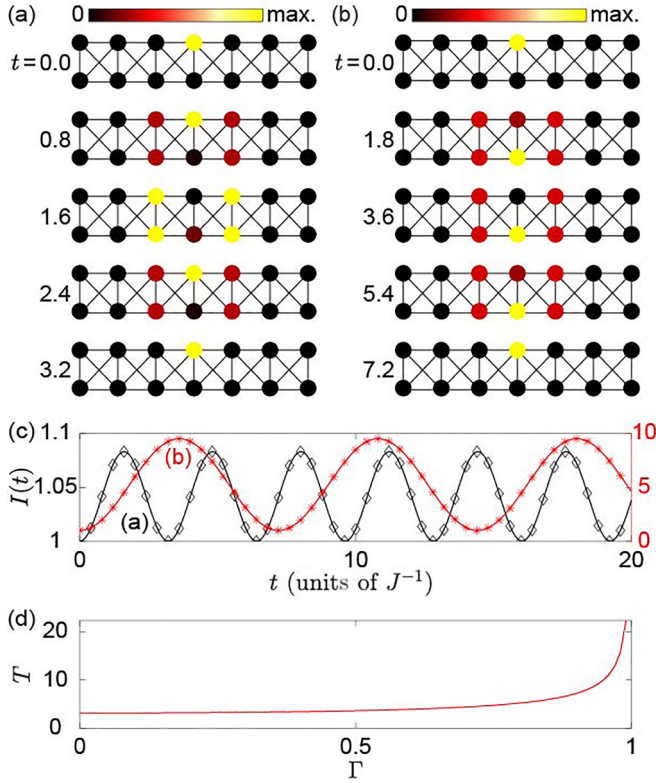


FIG. 4. (a), (b) Localization dynamics with normalized intensity for single-site excitations. The non-Hermitian Creutz ladder has $N = 7$ unit cells with 14 sites. (c) Intensity of the time-evolution dynamics. The initial excitation is at a single site shaded in yellow at $t = 0$. The parameters are fixed and being (a) $J = 1$, $\Gamma = 1/5$ and (b) $J = 1$, $\Gamma = 9/10$. The colored curves (marks) correspond to analytical (numerical) results of intensities. (d) Periodicity T with respect to the non-Hermiticity Γ , where $T = \pi/\sqrt{J^2 - \Gamma^2}$ and $\Gamma \in [0, 1)$.

For a single-site excitation at the upper leg of the Creutz ladder, the initial state is $\psi_1(0)$. Thus, the time-evolution state is

$$\begin{aligned} \psi_1(t) &= e^{-i\mathcal{H}t} \psi_1(0) \\ &= \left[\frac{iJ}{2\omega} \sin \omega t, -\frac{iJ}{2\omega} \sin \omega t, \cos \omega t, \right. \\ &\quad \left. -\frac{i\Gamma}{\omega} \sin \omega t, -\frac{iJ}{2\omega} \sin \omega t, -\frac{iJ}{2\omega} \sin \omega t \right]^T, \end{aligned} \quad (10)$$

where we set $\omega = \sqrt{J^2 - \Gamma^2}$ for simplicity. For a single-site excitation at the lower leg of the Creutz ladder, the initial state is $\psi_2(0)$, and the time-evolution state is

$$\begin{aligned} \psi_2(t) &= e^{-i\mathcal{H}t} \psi_2(0) \\ &= \left[\frac{iJ}{2\omega} \sin \omega t, -\frac{iJ}{2\omega} \sin \omega t, -\frac{i\Gamma}{\omega} \sin \omega t, \right. \\ &\quad \left. \cos \omega t, \frac{iJ}{2\omega} \sin \omega t, \frac{iJ}{2\omega} \sin \omega t \right]^T. \end{aligned} \quad (11)$$

Figures 4 and 5 depict the bounded intensity for the real spectrum at $J > \Gamma$. In contrast, in Fig. 6, the intensity is

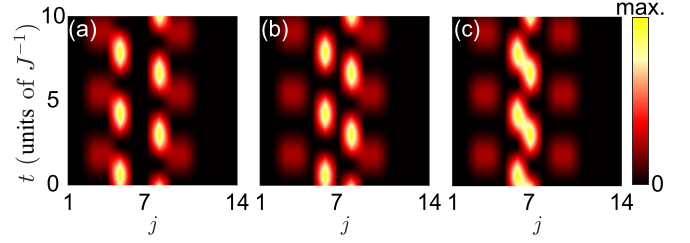


FIG. 5. The excitation confinement in the non-Hermitian Creutz ladder for the real spectrum at $J > \Gamma$. (a) The initial state is $[0, 0, 0, 0, 1, 0, 0, -1, 0, 0, 0, 0, 0, 0]^T/\sqrt{2}$. (b) The initial state is $[0, 0, 0, 0, 0, 1, 0, 1, 0, 0, 0, 0, 0, 0]^T/\sqrt{2}$. (c) The initial state is $[0, 0, 0, 0, 0, 1, 1, 0, 0, 0, 0, 0, 0, 0]^T/\sqrt{2}$. The system parameters are $J = 1$, $\Gamma = 1/2$, and $N = 7$.

unbounded and increases with time for the imaginary spectrum at $J < \Gamma$. Moreover, the time-evolution dynamics for any initial excitation can be analytically obtained from the superposition of these two types of single-site excitation dynamics.

In the following, we discuss the localization dynamics in two different phases in detail. In the case of $J > \Gamma$ with a fully flat spectrum, the remarkable feature of the non-Hermitian Creutz ladder is the oscillation period affected by Γ in the time-evolution process. Figure 4 performs numerical simulations of two types of single-site excitations, where the dynamics for the non-Hermitian Creutz ladder with the oscillation period $\pi/\sqrt{J^2 - \Gamma^2}$ can be observed. The non-Hermiticity plays a key role in extending the dynamic cycle. Moreover, the peculiar fusion phenomenon is depicted in Fig. 5 by changing the initial states, and the localization area ranges from sites 3 to 10 in all three panels.

In the case of $J < \Gamma$ with a fully imaginary spectrum, the non-Hermitian Creutz ladder exhibits a prominently surging intensity in the time-evolution dynamics. The confinement still remains because of the flatness of energy bands although the spectrum is not real. In Fig. 6, the normalized intensity is skillfully depicted to demonstrate the amplitudes, which eliminates the effect of sharply increased intensity and helps to clearly observe the dynamic change of wave-function amplitudes. Figure 6 shows the exotic phenomena of convergence, splitting and transfer during the evolution. The analytical time-evolution dynamics in Eqs. (10) and (11) helps to

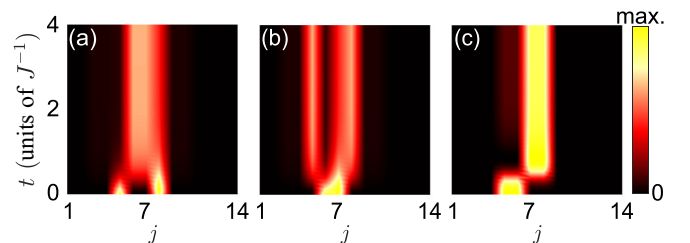


FIG. 6. The excitation confinement in the non-Hermitian Creutz ladder for the imaginary spectrum at $J < \Gamma$. The total intensity is normalized to unity. (a) The initial state is $[0, 0, 0, 0, 1, 0, 0, 1, 0, 0, 0, 0, 0, 0]^T/\sqrt{2}$. (b) The initial state is $[0, 0, 0, 0, 0, 1, -1, 0, 0, 0, 0, 0, 0, 0]^T/\sqrt{2}$. (c) The initial state is $[0, 0, 0, 0, 1, -1, 0, 0, 0, 0, 0, 0, 0, 0]^T/\sqrt{2}$. The system parameters are $J = 1$, $\Gamma = 3/2$, and $N = 7$.

obtain the results in Fig. 6. Since the time-evolution processes only involve several middle sites, the boundary condition has no influence on the localization behaviors. However, when considering an initial state excited at the lattice boundary, an intriguing phenomenon appears in the Creutz ladder under an open boundary condition.

Under the open boundary condition, the dynamic behavior concerning the edge state of the non-Hermitian Creutz ladder is also noteworthy, where the intensity may exponentially decay with time. This image, resulting from the boundary condition, breaks the inherent cognition that intensity increases with time in the time-evolution process. The normalized right edge state is $|\psi_R\rangle = [0, 0, \dots, 1, -1]^T/\sqrt{2}$ with the energy $-i\Gamma$ under open boundary condition, which is topologically protected due to the topological equivalence of the two lattices in Fig. 2. The time-evolution state $|\psi(t)\rangle$ for the initial state $|\psi_R\rangle$ is directly obtained, and expressed as $|\psi(t)\rangle = e^{-i\mathcal{H}t}|\psi_R\rangle = e^{-\Gamma t}[0, 0, \dots, 1, -1]^T/\sqrt{2}$. The time-evolution dynamics indicates that wave-function amplitudes only distribute on the right boundary. The corresponding intensity of the $|\psi(t)\rangle$ is $I(t) = e^{-2\Gamma t}$, which decreases sharply with time due to its exponential form. Moreover, the nonzero wave-function amplitudes only distribute for a short time, and the light propagation is interrupted under the open boundary condition. As for the left edge state $|\psi_L\rangle = [1, 1, \dots, 0, 0]^T/\sqrt{2}$ with energy $i\Gamma$, the exponentially increasing intensity of the time-evolution state is $I(t) = e^{2\Gamma t}$. As a comparison, intensities for two edge states at the dissipative coupling $-i\Gamma$ have opposite results under the open boundary condition. The decaying intensity $e^{-2\Gamma t}$ corresponds to the left edge state $|\psi_L\rangle$ with energy $-i\Gamma$, while the increasing intensity $e^{2\Gamma t}$ corresponds to the right edge state $|\psi_R\rangle$ with energy $i\Gamma$.

V. EXPERIMENTAL REALIZATION

The coupled resonator optical waveguides is a prominent platform for the realization of discrete lattice models and many intriguing phenomena in physics [110,111]. The coupled resonator optical waveguides are comprised of a sequence of ring resonators, where the high-precision modulation and manipulation of the light field are possible. Here, we propose the non-Hermitian Creutz ladder using the coupled resonator optical waveguides.

Figure 7(a) shows the schematic of a quasi-1D coupled ring resonator array, where the blue rings are the primary resonators, the cyan ellipses are the connecting waveguides, and the gray rings are the linking resonators. The primary resonators are indirectly coupled through the connecting waveguides and the linking resonators and the primary resonators on the upper and lower rows represent the sublattices *A* and *B*, respectively. The ring resonators support two degenerate clockwise and counterclockwise modes. The clockwise mode and the counterclockwise mode are decoupled. Notably, the mode chirality in the primary resonators and the mode chirality in the linking resonators are opposite.

Each connecting waveguide induces a nonreciprocal coupling $\pm iJ/2$ as shown in Fig. 7(b). The coupling is Hermitian and has a direction-dependent phase factor. The total length of the connecting waveguide is designed to allow the

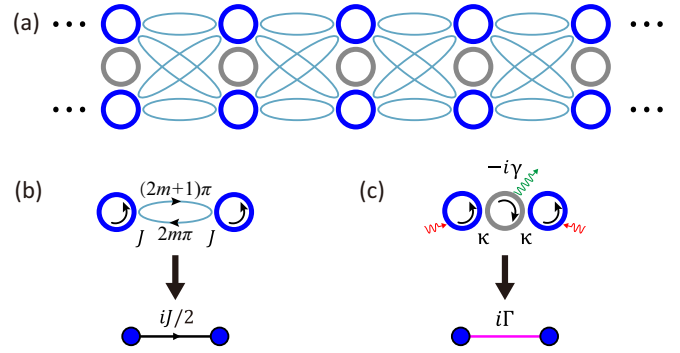


FIG. 7. (a) Schematic diagram of the coupled resonator optical waveguide. The primary resonators (blue rings) are coupled to each other via the connecting waveguides (cyan ellipses) and linking resonators (gray rings). (b) The realization of nonreciprocal Hermitian coupling $\pm iJ/2$, where photons tunneling between the resonators through the upper and lower paths along the connecting waveguide cumulate a phase factor of $e^{i(2m+1)\pi}$ and $e^{2m\pi}$, respectively. (c) The realization of reciprocal non-Hermitian coupling $i\Gamma$. Two primary resonators have the gain $i\Gamma$, the linking resonator has the loss $i\gamma$, the primary resonators and the linking resonator are coupled at the coupling strength κ .

accumulation of a phase shift of $e^{i(4m+1)\pi}$ when light propagates through it after a circle, where *m* is an integer. Such a design enables the constructive (destructive) interference of photons within the primary resonators (connecting waveguide). Consequently, the photons are confined in the primary resonators rather than the waveguides [112]. Furthermore, the lengths of the upper and lower branches of the connecting waveguide are different. The length difference causes a nonreciprocal phase. We consider all the primary resonators in the system are coupled to the connecting waveguides with identical coupling strength *J*. When a photon hops from the left resonator to the right resonator, it accumulates a different phase π than when the photon hops in the opposite direction. Thus, the nonreciprocal hopping phase factor is $e^{i\pi/2}$ for photons tunneling from left to right and is $e^{-i\pi/2}$ for photons tunneling from right to left. Thus, the primary resonators indirectly coupled through the connecting waveguides have the left to right coupling $+iJ/2$ and the right to left $-iJ/2$ according to coupled mode theory. The dynamics in the proposed coupled resonator optical waveguides are governed by the Hamiltonian of the Hermitian cross-stitch lattice.

To introduce the reciprocal non-Hermitian coupling $i\Gamma$, we use the linking resonator illustrated in Fig. 7(c) [82]. The linking resonators are designed to be on resonant with the primary resonators; and the linking resonators are evanescently coupled to the primary resonators with identical coupling strength κ . In the situation that the linking resonator is lossy with an attenuation rate $\gamma \gg \kappa$, the large dissipation enables the adiabatical elimination of the linking resonator light field and results in an effective coupling $i\Gamma$ between the primary resonators at the strength $\Gamma = \kappa^2/\gamma$. However, the common loss $-i\Gamma$ also appear on the two primary resonators after the adiabatic elimination process. Therefore, the extra gain $i\Gamma$ on the two primary resonators are required to balance the common loss $-i\Gamma$ induced by the linking resonator. The

dynamics in the proposed coupled resonator optical waveguides are governed by the Hamiltonian of the non-Hermitian Creutz ladder.

VI. CONCLUSION AND DISCUSSION

In this work, we propose an approach to construct the non-Hermitian AB cage through destructive interference, with the essential point being the formation of isolated non-Hermitian unit cells. We exemplify this approach by constructing a non-Hermitian Creutz ladder with dissipation-induced imaginary couplings introduced to the generalized cross-stitch lattice. The interplay between Hermiticity and non-Hermiticity affects the flat-band gap, compact localized states, and excitation confinement. The proposed non-Hermitian AB cage, not necessarily at the EP, enriches the dynamics of non-Hermitian localization. We offer an alternative solution and make a step forward in modulating the flat-band energy, manipulating the

light confinement, and steering the period of localization. Our approach to construct the non-Hermitian AB cage could be applicable for some other quasi-1D systems such as the rhombic lattice [18,47,48]. The non-Hermitian AB cage with desirable localization properties can be directly constructed by designing the decoupled non-Hermitian unit cells. Although the construction of non-Hermitian AB cages in two-dimensional and three-dimensional systems remains an open question, it is possible to generalize our idea to higher-dimensional systems. Alternatively, it is interesting to further consider the influence of the skin effect [113–116] and the nonlinear effect [16,17]. Our results may have potential applications for optical device design in the future.

ACKNOWLEDGMENT

We acknowledge the support of National Natural Science Foundation of China (Grant No. 11975128).

-
- [1] D. Leykam, A. Andreanov, and S. Flach, Artificial flat band systems: From lattice models to experiments, *Adv. Phys.* **X 3**, 1473052 (2018).
- [2] D. Leykam and S. Flach, Perspective: Photonic flatbands, *APL Photonics* **3**, 070901 (2018).
- [3] L. Morales-Inostroza and R. A. Vicencio, Simple method to construct flat-band lattices, *Phys. Rev. A* **94**, 043831 (2016).
- [4] A. Ramachandran, A. Andreanov, and S. Flach, Chiral flat bands: Existence, engineering, and stability, *Phys. Rev. B* **96**, 161104(R) (2017).
- [5] W. Maimaiti, S. Flach, and A. Andreanov, Universal $d = 1$ flatband generator from compact localized states, *Phys. Rev. B* **99**, 125129 (2019).
- [6] D. Yu, L. Yuan, and X. Chen, Isolated photonic flatband with the effective magnetic flux in a synthetic space including the frequency dimension, *Laser Photonics Rev.* **14**, 2000041 (2020).
- [7] W. Maimaiti, A. Andreanov, and S. Flach, Flat-band generator in two dimensions, *Phys. Rev. B* **103**, 165116 (2021).
- [8] H. Tasaki, Ferromagnetism in the Hubbard Models with Degenerate Single-Electron Ground States, *Phys. Rev. Lett.* **69**, 1608 (1992).
- [9] C. Wu, D. Bergman, L. Balents, and S. Das Sarma, Flat Bands and Wigner Crystallization in the Honeycomb Optical Lattice, *Phys. Rev. Lett.* **99**, 070401 (2007).
- [10] R. Mondaini, G. G. Batrouni, and B. Gremaud, Pairing and superconductivity in the flat band: Creutz lattice, *Phys. Rev. B* **98**, 155142 (2018).
- [11] S. Flach, D. Leykam, J. D. Bodyfelt, P. Matthies, and A. S. Desyatnikov, Detangling flat bands into Fano lattices, *Europhys. Lett.* **105**, 30001 (2014).
- [12] Y.-X. Xiao, G. Ma, Z.-Q. Zhang, and C. T. Chan, Topological Subspace-Induced Bound State in the Continuum, *Phys. Rev. Lett.* **118**, 166803 (2017).
- [13] C. Gneiting, Z. Li, and F. Nori, Lifetime of flatband states, *Phys. Rev. B* **98**, 134203 (2018).
- [14] L. Tang, D. Song, S. Xia, S. Xia, J. Ma, W. Yan, Y. Hu, J. Xu, D. Leykam, and Z. Chen, Photonic flat-band lattices and unconventional light localization, *Nanophotonics* **9**, 1161 (2020).
- [15] R. A. V. Pobleto, Photonic flat band dynamics, *Adv. Phys.: X* **6**, 1878057 (2021).
- [16] D. Leykam, O. Bahat-Treidel, and A. S. Desyatnikov, Pseudospin and nonlinear conical diffraction in Lieb lattices, *Phys. Rev. A* **86**, 031805(R) (2012).
- [17] D. Leykam, S. Flach, O. Bahat-Treidel, and A. S. Desyatnikov, Flat band states: Disorder and nonlinearity, *Phys. Rev. B* **88**, 224203 (2013).
- [18] G. Cáceres-Aravena, D. Guzmán-Silva, I. Salinas, and R. A. Vicencio, Controlled Transport Based on Multi-orbital Aharonov-Bohm Photonic Caging, *Phys. Rev. Lett.* **128**, 256602 (2022).
- [19] Y. Cao, V. Fatemi, S. Fang, K. Watanabe, T. Taniguchi, E. Kaxiras, and P. Jarillo-Herrero, Unconventional superconductivity in magic-angle graphene superlattices, *Nature (London)* **556**, 43 (2018).
- [20] M. Yankowitz, S. Chen, H. Polshyn, Y. Zhang, K. Watanabe, T. Taniguchi, D. Graf, A. F. Young, and C. R. Dean, Tuning superconductivity in twisted bilayer graphene, *Science* **363**, 1059 (2019).
- [21] L. Balents, C. R. Dean, D. K. Efetov, and A. F. Young, Superconductivity and strong correlations in moiré flat bands, *Nat. Phys.* **16**, 725 (2020).
- [22] A. Bermudez, D. Patanè, L. Amico, and M. A. Martin-Delgado, Topology-Induced Anomalous Defect Production by Crossing a Quantum Critical Point, *Phys. Rev. Lett.* **102**, 135702 (2009).
- [23] K. Sun, Z. Gu, H. Katsura, and S. D. Sarma, Nearly Flatbands with Nontrivial Topology, *Phys. Rev. Lett.* **106**, 236803 (2011).
- [24] E. Tang, J.-W. Mei, and X.-G. Wen, High-Temperature Fractional Quantum Hall States, *Phys. Rev. Lett.* **106**, 236802 (2011).
- [25] T. Neupert, L. Santos, C. Chamon, and C. Mudry, Fractional Quantum Hall States at Zero Magnetic Field, *Phys. Rev. Lett.* **106**, 236804 (2011).

- [26] S. Mukherjee, A. Spracklen, D. Choudhury, N. Goldman, P. Öhberg, E. Andersson, and R. R. Thomson, Observation of a Localized Flat-Band State in a Photonic Lieb Lattice, *Phys. Rev. Lett.* **114**, 245504 (2015).
- [27] R. A. Vicencio, C. Cantillano, L. Morales-Inostroza, B. Real, C. Mejía-Cortés, S. Weimann, A. Szameit, and M. I. Molina, Observation of Localized States in Lieb Photonic Lattices, *Phys. Rev. Lett.* **114**, 245503 (2015).
- [28] S. Mukherjee and R. R. Thomson, Observation of robust flat band localization in driven photonic rhombic lattices, *Opt. Lett.* **42**, 2243 (2017).
- [29] S. Mukherjee, M. D. Liberto, P. Öhberg, R. R. Thomson, and N. Goldman, Experimental Observation of Aharonov-Bohm Cages in Photonic Lattices, *Phys. Rev. Lett.* **121**, 075502 (2018).
- [30] G.-B. Jo, J. Guzman, C. K. Thomas, P. Hosur, A. Vishwanath, and D. M. Stamper-Kurn, Ultracold Atoms in a Tunable Optical Kagome Lattice, *Phys. Rev. Lett.* **108**, 045305 (2012).
- [31] S. Taie, H. Ozawa, T. Ichinose, T. Nishio, S. Nakajima, and Y. Takahashi, Coherent driving and freezing of bosonic matterwave in an optical Lieb lattice, *Sci. Adv.* **1**, e1500854 (2015).
- [32] R. Drost, T. Ojanen, A. Harju, and P. Liljeroth, Topological states in engineered atomic lattices, *Nat. Phys.* **13**, 668 (2017).
- [33] N. Masumoto, N. Y. Kim, T. Byrnes, K. Kusudo, A. Löffler, S. Höfling, A. Forchel, and Y. Yamamoto, Exciton-polariton condensates with flat bands in a two-dimensional kagome lattice, *New J. Phys.* **14**, 065002 (2012).
- [34] Y. Nakata, T. Okada, T. Nakanishi, and M. Kitano, Observation of flat band for terahertz spoof plasmons in a metallic kagomé lattice, *Phys. Rev. B* **85**, 205128 (2012).
- [35] S. Kajiwara, Y. Urade, Y. Nakata, T. Nakanishi, and M. Kitano, Observation of a nonradiative flat band for spoof surface plasmons in a metallic Lieb lattice, *Phys. Rev. B* **93**, 075126 (2016).
- [36] M. R. Slot, T. S. Gardenier, P. H. Jacobse, G. C. P. van Miert, S. N. Kempkes, S. J. M. Zevenhuizen, C. M. Smith, D. Vanmaekelbergh, and I. Swart, Experimental realization and characterization of an electronic Lieb lattice, *Nat. Phys.* **13**, 672 (2017).
- [37] C. E. Whittaker, E. Cancellieri, P. M. Walker, D. R. Gulevich, H. Schomerus, D. Vaitiekus, B. Royall, D. M. Whittaker, E. Clarke, I. V. Iorsh, I. A. Shelykh, M. S. Skolnick, and D. N. Krizhanovskii, Exciton Polaritons in a Two-Dimensional Lieb Lattice with Spin-Orbit Coupling, *Phys. Rev. Lett.* **120**, 097401 (2018).
- [38] B. C. Xu, B. Y. Xie, L. H. Xu, M. Deng, W. J. Chen, H. Wei, F. L. Dong, J. Wang, C. W. Qiu, S. Zhang, and L. Chen, Topological Landau-Zener nanophotonic circuits, *Adv. Photon.* **5**, 036005 (2023).
- [39] Y. He, R. Mao, H. Cai, J.-X. Zhang, Y. Li, L. Yuan, S.-Y. Zhu, and D.-W. Wang, Flat-Band Localization in Creutz Superradiance Lattices, *Phys. Rev. Lett.* **126**, 103601 (2021).
- [40] S. Longhi, Aharonov-Bohm photonic cages in waveguide and coupled resonator lattices by synthetic magnetic fields, *Opt. Lett.* **39**, 5892 (2014).
- [41] S. Mukherjee and R. R. Thomson, Observation of localized flat-band modes in a quasi-one-dimensional photonic rhombic lattice, *Opt. Lett.* **40**, 5443 (2015).
- [42] J. Vidal, R. Mosseri, and B. Douçot, Aharonov-Bohm Cages in Two-Dimensional Structures, *Phys. Rev. Lett.* **81**, 5888 (1998).
- [43] C. Naud, G. Faini, and D. Maily, Aharonov-Bohm Cages in 2D Normal Metal Networks, *Phys. Rev. Lett.* **86**, 5104 (2001).
- [44] D. Bercioux, D. F. Urban, H. Grabert, and W. Häusler, Massless Dirac-Weyl fermions in a \mathcal{T}_3 optical lattice, *Phys. Rev. A* **80**, 063603 (2009).
- [45] D. Bercioux, N. Goldman, and D. F. Urban, Topology-induced phase transitions in quantum spin Hall lattices, *Phys. Rev. A* **83**, 023609 (2011).
- [46] S. M. Zhang and L. Jin, Compact localized states and localization dynamics in the dice lattice, *Phys. Rev. B* **102**, 054301 (2020).
- [47] M. Kremer, I. Petrides, E. Meyer, M. Heinrich, O. Zilberberg, and A. Szameit, A square-root topological insulator with non-quantized indices realized with photonic Aharonov-Bohm cages, *Nat. Commun.* **11**, 907 (2020).
- [48] C. Jörg, G. Queraltó, M. Kremer, G. Pelegrí, J. Schulz, A. Szameit, G. V. Freymann, J. Mompert, and V. Ahufinger, Artificial gauge field switching using orbital angular momentum modes in optical waveguides, *Light Sci. Appl.* **9**, 150 (2020).
- [49] M. Di Liberto, S. Mukherjee, and N. Goldman, Nonlinear dynamics of Aharonov-Bohm cages, *Phys. Rev. A* **100**, 043829 (2019).
- [50] G. Gligorić, D. Leykam, and A. Maluckov, Influence of different disorder types on Aharonov-Bohm caging in the diamond chain, *Phys. Rev. A* **101**, 023839 (2020).
- [51] N. Chang, S. Gundogdu, D. Leykam, D. G. Angelakis, S. Kou, S. Flach, and A. Maluckov, Nonlinear Bloch wave dynamics in photonic Aharonov-Bohm cages, *APL Photon.* **6**, 030801 (2021).
- [52] G. Pelegrí, A. M. Marques, R. G. Dias, A. J. Daley, J. Mompert, and V. Ahufinger, Topological edge states and Aharonov-Bohm caging with ultracold atoms carrying orbital angular momentum, *Phys. Rev. A* **99**, 023613 (2019).
- [53] S. Longhi, Photonic flat-band laser, *Opt. Lett.* **44**, 287 (2019).
- [54] Y. Kuno, T. Mizoguchi, and Y. Hatsugai, Interaction-induced doublons and embedded topological subspace in a complete flat-band system, *Phys. Rev. A* **102**, 063325 (2020).
- [55] A. Mukherjee, A. Nandy, S. Sil, and A. Chakrabarti, Tailoring flat bands and topological phases in a multistrand Creutz network, *Phys. Rev. B* **105**, 035428 (2022).
- [56] J. S. C. Hung, J. H. Busnaina, C. W. S. Chang, A. M. Vadiraj, I. Nsanzineza, E. Solano, H. Alaeian, E. Rico, and C. M. Wilson, Quantum Simulation of the Bosonic Creutz Ladder with a Parametric Cavity, *Phys. Rev. Lett.* **127**, 100503 (2021).
- [57] T. Orito, Y. Kuno, and I. Ichinose, Interplay and competition between disorder and flat band in an interacting Creutz ladder, *Phys. Rev. B* **104**, 094202 (2021).
- [58] J. Zurita, C. E. Creffield, and G. Platero, Topology and interactions in the photonic creutz and creutz-hubbard ladders, *Adv. Quantum Technol.* **3**, 1900105 (2020).
- [59] L. Jin and Z. Song, Solutions of \mathcal{PT} -symmetric tight-binding chain and its equivalent Hermitian counterpart, *Phys. Rev. A* **80**, 052107 (2009).
- [60] Y. D. Chong, L. Ge, H. Cao, and A. D. Stone, Coherent Perfect Absorbers: Time-Reversed Lasers, *Phys. Rev. Lett.* **105**, 053901 (2010).

- [61] S. Longhi, \mathcal{PT} -symmetric laser absorber, *Phys. Rev. A* **82**, 031801(R) (2010).
- [62] C. E. Rüter, K. G. Makris, R. El-Ganainy, D. N. Christodoulides, M. Segev, and D. Kip, Observation of parity-time symmetry in optics, *Nat. Phys.* **6**, 192 (2010).
- [63] K. Ding, C. Fang, and G. Ma, Non-Hermitian topology and exceptional-point geometries, *Nat. Rev. Phys.* **4**, 745 (2022).
- [64] A. Li, H. Wei, M. Cotrufo, W. Chen, S. Mann, X. Ni, B. Xu, J. Chen, J. Wang, S. Fan, C.-W. Qiu, A. Alù, and L. Chen, Exceptional points and non-Hermitian photonics at the nanoscale, *Nat. Nanotechnol.* **18**, 706 (2023).
- [65] L. Jin and Z. Song, Incident Direction Independent Wave Propagation and Unidirectional Lasing, *Phys. Rev. Lett.* **121**, 073901 (2018).
- [66] H. S. Xu and L. Jin, Coupling-induced nonunitary and unitary scattering in anti- \mathcal{PT} -symmetric non-Hermitian systems, *Phys. Rev. A* **104**, 012218 (2021).
- [67] H. S. Xu, L. C. Xie, and L. Jin, High-order spectral singularity, *Phys. Rev. A* **107**, 062209 (2023).
- [68] L. Jin and Z. Song, Bulk-boundary correspondence in a non-Hermitian system in one dimension with chiral inversion symmetry, *Phys. Rev. B* **99**, 081103(R) (2019).
- [69] S. M. Zhang, X. Z. Zhang, L. Jin, and Z. Song, High-order exceptional point in supersymmetric array, *Phys. Rev. A* **101**, 033820 (2020).
- [70] H. C. Wu, X. M. Yang, L. Jin, and Z. Song, Untying links through anti-parity-time-symmetric coupling, *Phys. Rev. B* **102**, 161101(R) (2020).
- [71] H. C. Wu, L. Jin, and Z. Song, Topology of an anti-parity-time symmetric non-Hermitian Su-Schrieffer-Heeger model, *Phys. Rev. B* **103**, 235110 (2021).
- [72] H. Ramezani, Non-Hermiticity-induced flat band, *Phys. Rev. A* **96**, 011802(R) (2017).
- [73] D. Leykam, S. Flach, and Y. D. Chong, Flat bands in lattices with non-Hermitian coupling, *Phys. Rev. B* **96**, 064305 (2017).
- [74] B. Qi, L. Zhang, and L. Ge, Defect States Emerging from a Non-Hermitian Flat Band of Photonic Zero Modes, *Phys. Rev. Lett.* **120**, 093901 (2018).
- [75] A. A. Zyuzin and A. Yu. Zyuzin, Flat band in disorder-driven non-Hermitian Weyl semimetals, *Phys. Rev. B* **97**, 041203(R) (2018).
- [76] L. Ge, Non-Hermitian lattices with a flat band and polynomial power increase, *Photon. Res.* **6**, A10 (2018).
- [77] S. M. Zhang and L. Jin, Flat band in two-dimensional non-Hermitian optical lattices, *Phys. Rev. A* **100**, 043808 (2019).
- [78] L. Jin, Flat band induced by the interplay of synthetic magnetic flux and non-Hermiticity, *Phys. Rev. A* **99**, 033810 (2019).
- [79] S. M. Zhang and L. Jin, Localization in non-Hermitian asymmetric rhombic lattice, *Phys. Rev. Res.* **2**, 033127 (2020).
- [80] P. He, H.-T. Ding, and S.-L. Zhu, Geometry and superfluidity of the flat band in a non-Hermitian optical lattice, *Phys. Rev. A* **103**, 043329 (2021).
- [81] W. Maimaiti and A. Andreanov, Non-Hermitian flat-band generator in one dimension, *Phys. Rev. B* **104**, 035115 (2021).
- [82] L. Ding, Z. Lin, S. Ke, B. Wang, and P. Lu, Non-Hermitian flat bands in rhombic microring resonator arrays, *Opt. Express* **29**, 24373 (2021).
- [83] D. Leykam, K. Y. Bliokh, C. Huang, Y. D. Chong, and F. Nori, Edge Modes, Degeneracies, and Topological Numbers in Non-Hermitian Systems, *Phys. Rev. Lett.* **118**, 040401 (2017).
- [84] D. Leykam, V. V. Konotop, and A. S. Desyatnikov, Discrete vortex solitons and parity time symmetry, *Opt. Lett.* **38**, 371 (2013).
- [85] S. Ke, D. Zhao, J. Fu, Q. Liao, B. Wang, and P. Lu, Topological edge modes in non-hermitian photonic aharonov-bohm cages, *IEEE J. Sel. Top. Quantum Electron.* **26**, 4401008 (2020).
- [86] R. Nehra, D. S. Bhakuni, A. Ramachandran, and A. Sharma, Flat bands and entanglement in the Kitaev ladder, *Phys. Rev. Res.* **2**, 013175 (2020).
- [87] S. M. Chan, B. Grémaud, and G. G. Batrouni, Pairing and superconductivity in quasi-one-dimensional flat-band systems: Creutz and sawtooth lattices, *Phys. Rev. B* **105**, 024502 (2022).
- [88] Y. Kuno, Extended flat band, entanglement, and topological properties in a Creutz ladder, *Phys. Rev. B* **101**, 184112 (2020).
- [89] F. Yang, Y.-C. Liu, and L. You, Anti- \mathcal{PT} symmetry in dissipatively coupled optical systems, *Phys. Rev. A* **96**, 053845 (2017).
- [90] V. V. Konotop and D. A. Zezyulin, Odd-Time Reversal \mathcal{PT} Symmetry Induced by an Anti- \mathcal{PT} -Symmetric Medium, *Phys. Rev. Lett.* **120**, 123902 (2018).
- [91] Y. Yang, X. Xie, Y. Li, Z. Zhang, Y. Peng, C. Wang, E. Li, Y. Li, H. Chen, and F. Gao, Radiative anti-parity-time plasmonics, *Nat. Commun.* **13**, 7678 (2022).
- [92] F. Zhang, Y. Feng, X. Chen, L. Ge, and W. Wan, Synthetic Anti-PT Symmetry in a Single Microcavity, *Phys. Rev. Lett.* **124**, 053901 (2020).
- [93] W. Liu, Y. Zhang, Z. Deng, J. Ye, K. Wang, B. Wang, D. Gao, and P. Lu, On-chip chiral mode switching by encircling an exceptional point in an anti-parity-time symmetric system, *Laser Photonics Rev.* **16**, 2100675 (2022).
- [94] A. Bergman, R. Duggan, K. Sharma, M. Tur, A. Zadok, and A. Alù, Observation of anti-parity-time-symmetry, phase transitions and exceptional points in an optical fibre, *Nat. Commun.* **12**, 486 (2021).
- [95] Y. Li, Y.-G. Peng, L. Han, M.-A. Miri, W. Li, M. Xiao, X.-F. Zhu, J. Zhao, A. Alù, S. Fan, and C.-W. Qiu, Anti-parity-time symmetry in diffusive systems, *Science* **364**, 170 (2019).
- [96] Y. Yang, Y.-P. Wang, J. W. Rao, Y. S. Gui, B. M. Yao, W. Lu, and C.-M. Hu, Unconventional Singularity in Anti-Parity-Time Symmetric Cavity Magnonics, *Phys. Rev. Lett.* **125**, 147202 (2020).
- [97] J. Zhao, Y. Liu, L. Wu, C.-K. Duan, Y.-X. Liu, and J. Du, Observation of Anti- \mathcal{PT} -Symmetry Phase Transition in the Magnon-Cavity-Magnon Coupled System, *Phys. Rev. Appl.* **13**, 014053 (2020).
- [98] X. Wang and J.-H. Wu, Optical \mathcal{PT} -symmetry and \mathcal{PT} -antisymmetry in coherently driven atomic lattices, *Opt. Express* **24**, 4289 (2016).
- [99] Y. Jiang, Y. Mei, Y. Zuo, Y. Zhai, J. Li, J. Wen, and S. Du, Anti-Parity-Time Symmetric Optical Four-Wave Mixing in Cold Atoms, *Phys. Rev. Lett.* **123**, 193604 (2019).
- [100] Y. Choi, C. Hahn, J. W. Yoon, and S. H. Song, Observation of an anti-PT-symmetric exceptional point and energy-difference conserving dynamics in electrical circuit resonators, *Nat. Commun.* **9**, 2182 (2018).
- [101] H. Li, A. Mekawy, and A. Alù, Gain-Free Parity-Time Sym-

- metry for Evanescent Fields, *Phys. Rev. Lett.* **127**, 014301 (2021).
- [102] Z. Xiao and A. Alù, Tailoring exceptional points in a hybrid \mathcal{PT} -symmetric and anti- \mathcal{PT} -symmetric scattering system, *Nanophotonics* **10**, 3723 (2021).
- [103] J. Akram and C. Zheng, Theoretical investigation of dynamics and concurrence of entangled \mathcal{PT} and anti- \mathcal{PT} symmetric polarized photons, *Sci. Rep.* **13**, 8542 (2023).
- [104] P. Peng, W. Cao, C. Shen, W. Qu, J. Wen, L. Jiang, and Y. Xiao, Anti-parity-time symmetry with flying atoms, *Nat. Phys.* **12**, 1139 (2016).
- [105] H. Zhang, R. Huang, S.-D. Zhang, Y. Li, C.-W. Qiu, F. Nori, and H. Jing, Breaking anti- \mathcal{PT} symmetry by spinning a resonator, *Nano Lett.* **20**, 7594 (2020).
- [106] J. Zhang, Z. Feng, and X. Sun, Realization of bound states in the continuum in anti- \mathcal{PT} -symmetric optical systems: A proposal and analysis, *Laser Photonics Rev.* **17**, 2200079 (2023).
- [107] X.-L. Zhang, T. Jiang, and C. T. Chan, Dynamically encircling an exceptional point in anti-parity-time symmetric systems: Asymmetric mode switching for symmetry-broken modes, *Light Sci. Appl.* **8**, 88 (2019).
- [108] Z. Feng and X. Sun, Harnessing Dynamical Encircling of an Exceptional Point in Anti- \mathcal{PT} -Symmetric Integrated Photonic Systems, *Phys. Rev. Lett.* **129**, 273601 (2022).
- [109] S. Ke, D. Zhao, J. Liu, Q. Liu, Q. Liao, B. Wang, and P. Lu, Topological bound modes in anti- \mathcal{PT} -symmetric optical waveguide arrays, *Opt. Express* **27**, 13858 (2019).
- [110] H. S. Xu and L. Jin, Coherent resonant transmission, *Phys. Rev. Res.* **4**, L032015 (2022).
- [111] L. Xie, L. Jin, and Z. Song, Antihelical edge states in two-dimensional photonic topological metals, *Sci. Bull.* **68**, 255 (2023).
- [112] M. Hafezi, E. A. Demler, M. D. Lukin, and J. M. Taylor, Robust optical delay lines with topological protection, *Nat. Phys.* **7**, 907 (2011).
- [113] R. Lin, T. Tai, L. Li, and C. H. Lee, Topological non-Hermitian skin effect, *Front. Phys.* **18**, 53605 (2023).
- [114] S. L. Ke, W. T. Wen, D. Zhao, and Y. Wang, Floquet engineering of the non-Hermitian skin effect in photonic waveguide arrays, *Phys. Rev. A* **107**, 053508 (2023).
- [115] F. Qin, Y. Ma, R. Z. Shen, and C. H. Lee, Universal competitive spectral scaling from the critical non-Hermitian skin effect, *Phys. Rev. B* **107**, 155430 (2023).
- [116] W. W. Zhu and J. B. Gong, Photonic corner skin modes in non-Hermitian photonic crystals, *Phys. Rev. B* **108**, 035406 (2023).